Advances in Water Resources 105 (2017) 29–38

Contents lists available at ScienceDirect

Advances in Water Resources

journal homepage: www.elsevier.com/locate/advwatres

Modeling variability in porescale multiphase flow experiments

Bowen Ling[a,b], Jie Bao[c], Mart Oostrom[c], Ilenia Battiato[d], Alexandre M. Tartakovsky[c,*]

[a] Mechanical and Aerospace Engineering, University of California San Diego, San Diego, CA, USA
[b] Mechanical Engineering, San Diego State University, San Diego, CA, USA
[c] Pacific Northwest National Laboratory, Richland, WA, USA
[d] Energy Resources Engineering, Stanford University, Stanford, CA, USA

ARTICLE INFO

Article history:
Received 11 November 2016
Revised 6 April 2017
Accepted 10 April 2017
Available online 11 April 2017

Keywords:
Multiphase flow experiments
Pore-scale simulation
Volume of fluids

ABSTRACT

Microfluidic devices and porescale numerical models are commonly used to study multiphase flow in biological, geological, and engineered porous materials. In this work, we perform a set of drainage and imbibition experiments in six identical microfluidic cells to study the reproducibility of multiphase flow experiments. We observe significant variations in the experimental results, which are smaller during the drainage stage and larger during the imbibition stage. We demonstrate that these variations are due to sub-porescale geometry differences in microcells (because of manufacturing defects) and variations in the boundary condition (i.e., fluctuations in the injection rate inherent to syringe pumps). Computational simulations are conducted using commercial software STAR-CCM+, both with constant and randomly varying injection rates. Stochastic simulations are able to capture variability in the experiments associated with the varying pump injection rate.

1. Introduction

In the last several decades, porescale two-phase flow has attracted significant attention (Blunt, 2001; Hassanizadeh and Gray, 1990; Lenormand et al., 1988; 1983; Sahimi, 2011). At the pore scale, multiphase flow is governed by the Navier–Stokes (NS) equations subject to the Young–Laplace boundary condition at the fluid-fluid interface and the Young condition at the fluid-fluid-solid interface (Young, 1805). These equations are highly non-linear because of the moving fluid-fluid and fluid-fluid-solid boundaries, which presents a significant challenge for obtaining accurate numerical solutions (Miller et al., 1998; Tartakovsky and Panchenko, 2016). A number of mathematical formulations have been proposed to simplify the solution of these equations, including methods that describe interface dynamics implicitly by means of a "color" function (Wachem and Almstedt, 2003) (e.g., the volume of fluid (Hirt and Nichols, 1981), density functional method, and phase-field method (Steinbach et al., 1996)). Various formulations have been used to describe the dynamics of a fluid-fluid-solid interface, including static and dynamic contact angles, energy-balance considerations, and pairwise forces. Various numerical methods, including mesh-based finite volume and mesh-less Smoothed Particle Hydrodynamics, have been used to solve the resulting Navier–Stokes equations. Other (so-called "mesoscale") methods (e.g., Lattice-Boltzmann and Dissipative Particle Dynamics) also have been applied to model multiphase flow in porous media. The resulting models have different degrees of complexity in representing fluid-fluid-solid interactions, numerical accuracy, and the computational cost (for a review of numerical methods for multiphase porescale flow, see Meakin and Tartakovsky, 2009).

A natural question to ask is, what model complexity and numerical accuracy are sufficient to correctly model multiphase flow on the pore scale? The qualifier "correctly" in this question is important because, in many studies, the porescale models are verified and validated only in a "weak" sense, i.e., by comparing the average solution (or its properties, such as pressure-saturation relationship) obtained from a numerical model and the corresponding experiment (e.g., Bandara et al., 2013; Liu et al., 2014; Pan et al., 2004). Not that the comparison of average properties of solutions lacks merit; however, it is also reasonable to require a porescale numerical model to reproduce porescale properties of the solution accurately. Comparison with well-controlled, porescale multiphase flow experiments is a reasonable way to validate and verify a numerical model. The answer to the preceeding question is complicated by, at least, three factors: 1) depending on the initial and boundary conditions, the equations describing multiphase flow could be unstable, i.e., small perturbations in initial and boundary conditions may lead to large differences in the solution; 2) the exact geometry and roughness of the flow domain boundaries (i.e., the pore geometry), even when possible to precisely measure, are

* Corresponding author.
E-mail address: alexandre.tartakovsky@pnnl.gov (A.M. Tartakovsky).

http://dx.doi.org/10.1016/j.advwatres.2017.04.005
0309-1708/

usually impractical to fully resolve; and 3) initial conditions are difficult to control in an experiment and exactly reproduce in the numerical model. Still, even if these challenges could be overcome, reproducible experimental results are needed to conduct a validation study.

Quasi-two-dimensional microfluidic cells are often used to experimentally study porescale flow (Cottin et al., 2010; Zhang et al., 2011a; 2011b). They afford better control and monitoring of flow dynamics than three-dimensional small-column experiments. Therefore, the microcell experiments are perfect candidates to generate results for a validation study. Often, microfluidic studies use a pore geometry made of a uniform array of cylinders (e.g., Zhang et al., 2011b). Multiphase flows in such pore structures are particularly difficult to reproduce in both experiments and numerical simulations for several reasons: 1) small manufacturing defects break "symmetry" and significantly affect the multiphase flow; 2) even if the actual manufactured geometry could be exactly measured, the differences between the prescribed (design) and actual geometry could be impractical to resolve in a numerical model; and 3) small time-variations in the flux rate generated by syringe pumps may lead to significant changes in the final distribution of fluid phases. In Ferrari et al. (2015), multiphase flow in both heterogeneous and homogeneous pore structures was studied, and the "point-by-point" difference in displacement patterns, obtained experimentally and numerically, was found to be from 17 to 30% in the heterogeneous porous structure and from 30 to 40% in the homogeneous domain, depending on a numerical model used. The reproducibility of experimental results was not addressed in Ferrari et al. (2015).

In the first part of this work, we study the question of reproducibility of experiments by repeating simulations in six microcells with the same (up to the manufacturing error) geometry. We use a highly non-uniform pore-size distribution to minimize the effect of small deviations from the design pore geometry and injection rate on the experimental results. In all experiments, a microcell is initially occupied with a wetting fluid, and a non-wetting fluid is injected through the left boundary for 30 s with a constant flux q using a high-precision pump (variations in the injections rate are less than 5% per manufacturer's specification). Then, a wetting fluid is injected through the right port until the saturation of the non-wetting fluid reaches steady state. Our study shows a significant variability in the porescale distribution of fluid phases, interface area, and saturation. In the second part of our study, we conduct two- and three-dimensional simulations with constant and randomly varying injection rates to capture average behavior and variability observed in the experiments. We use a commercial finite volume code STAR-CCM+ (CD-adapco, Melville, NY, USA) in our numerical study. Our results show that the three-dimensional simulation with a deterministic flux q better captures the mean behavior observed in the experiment than the two-dimensional model (which disregards the effect of the interface curvature in a plane perpendicular to the microcell top and bottom walls) with the constant q. The two-dimensional simulations with randomly varying (around the prescribed in the experiments) flux capture the variability observed in the experiments, but the average behaviors found in the simulations and experiments differ. We also find that the average behavior of stochastic simulations differs from the corresponding deterministic simulations because of strong non-linearity of the governing equations.

2. Microfluidic experiments

2.1. Design and photolithography

The reproducibility of porescale multiphase flow experiments is investigated in a microfluidic device shown in Fig. 1-a. For this study, six replicas of the device are manufactured and up to five experiments are conducted for each replica. To minimize the effect of pore-geometry deviations (manufacturing defects) from the prescribed geometry, porescale heterogeneity is introduced in the form of a preferential flow path with a width w_{t1}. Tubes (or pipes) are connected to the inlet and outlet, which have the width w_{t2}. The design dimensions of the micromodel are provided in Table 1.

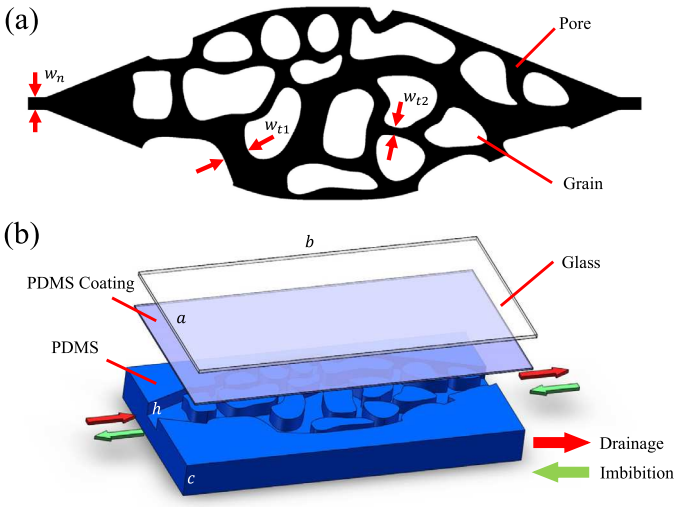

Fig. 1. (a) Pore structure. Pore spaces are shown in black, and the solid phase is in white; (b) Three-dimensional configuration.

Table 1
Micromodel dimensions.

Symbols (Fig. 1)	Length (mm)
$a \times b \times c$	$5 \times 18 \times 5$
h	0.03
w_n	0.1
w_{t1}	$\sim$ 0.4–0.5
w_{t2}	$\sim$ 0.1

The micromodels (Fig. 1-b) are fabricated using standard photolithographic techniques. The six replicas of the design pore geometry are printed on a single photomask. Then, an SU-8 negative photo-resistant material is coated onto a 4-inch diameter silicon wafer. The cell base is made from the hydrophobic polydimethylsiloxane (PDMS) material "baked" in an oven for over 12 h at 75 °C (Fig. 1-b). To make the wetting properties of the cell's glass top the same as that of the PDMS base, the glass is also coated with a thin layer of PDMS. To achieve chemically stable hydrophobic interior surfaces, the assembled cells are placed for an additional 48 h in an oven at 200 °C.

2.2. Experimental design

The fluids are injected and removed from a micromodel using a piping system shown in Fig. 2. To perform drainage and imbibition phases of the experiment, glass syringes (1 mL Glass Syringe, Hamilton) containing the wetting fluid (hexadecane) and the non-wetting fluid (DI-water) are used. A series of valves are used to enable and disable flow paths during these phases (Fig. 2-c). This experimental design allows for a smooth switching from the drainage to the imbibition phase without cross-contamination while preventing formation of air bubbles. A precision syringe pump (NE-4002X, New Era Pump System) is used to produce a constant injection rate.

To conduct an experiment, a micromodel is placed horizontally on a microscope stage (Prior Scientific Instruments LTD.) to

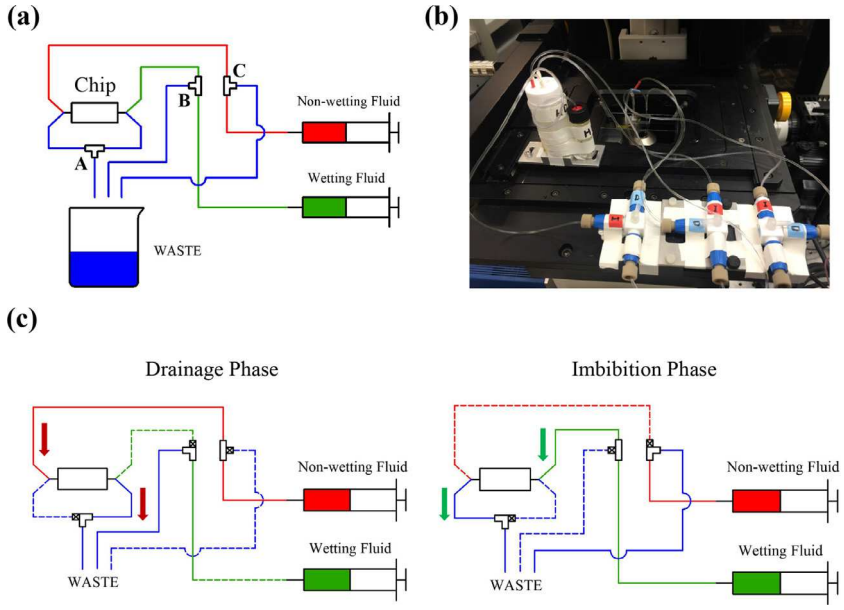

Fig. 2. (a) Illustration of the piping system; (b) Realization; (c) Flow path in different phases of the experiment.

minimize the effect of gravity. Fluid displacement is visualized by a microscope (Nikon Eclipse-2000TiE) with a 4 × magnifying lens and a 3.23 μm spatial resolution. Light is provided by a high-intensity light source (Nikon Intensilight C-HGFIE), and images are recorded using a monochrome digital charge-coupled device (CCD) camera. All devices are connected to a computer, and the recording speed, exposure time, and shutter time are set by the imaging software NIS-Elements (Nikon). The resulting exposure time for taking images is ≈ 1 ms, which is small enough to prevent changes in fluid properties due to heating and light exposure. Before the start of each experiment, the micromodel is first saturated with the wetting fluid (hexadecane). Then, during the drainage phase, the non-wetting fluid (DI water) is injected for 30 s. Subsequently, the piping system is switched for imbibition, and the wetting fluid is injected for 40 s. The results of the imbibition part of the experiment are reported after 30 s from the start of the wetting fluid injection.

The time for the drainage cycle is determined from a test drainage experiment. Fig. 4 shows the saturation as a function of time observed in this experiment. It can be seen that the saturation of the injected non-wetting fluid almost reaches steady state after 30 s. Fig. 5 depicts saturation as a function of time during a typical drainage-imbibition experiment discussed in the paper. The drainage is conducted for 30 s, then the system is given approximately 8 s to relax, after which the imbibition experiment is performed for more than 40 s. Here, as in the test drainage experiment, the saturation almost reaches steady state after 30 s. The saturation practically does not change during the relaxation period. During the imbibition stage, the saturation reaches steady state after less than 25 s. Based on this, all results of the imbibition experiments are reported after 30 s. There is a small increase in the saturation after the start of imbibition due to some non-wetting fluid left in the right-hand-side pipes and being pushed back by the imbibing wetting fluid.

Table 2 includes the properties of both fluids, prescribed injection velocity, and the resulting viscosity ratio ($M = \mu_{nw}/\mu_w$) and capillary number ($Ca = \mu_{nw}U/\sigma$). The static contact angle (θ) between the two fluids and PDMS surface is measured in the cell inlet (Fig. 3) from an auxiliary experiment where wetting fluid is injected for a short period of time. The measured values of θ are between 16° to 18°, with an averaged value of 16.8°. The selected

Table 2
Wetting (hexadecane) and non-wetting (DI water) fluid properties.

Property	Value
Non-wetting fluid viscosity (μ_{nw}, cP)	1.02
Wetting fluid viscosity (μ_w, cP)	3.34
Surface tension (σ, mN/m)	52.00
Contact angle (θ, deg)	16.79
Injection velocity (U, m/s)	9.24×10^{-4}
$log(M)$	−0.51
$log(Ca)$	−4.74

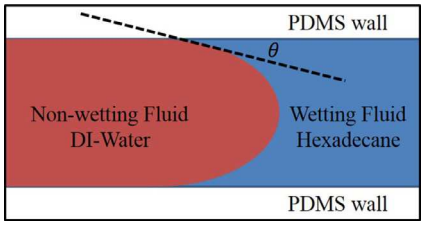

Fig. 3. Definition of the non-wetting/wetting fluid and contact angle.

Ca and *M* numbers put the studied flow in an unstable displacement regime on the boundary of viscous and capillary fingering regimes according to the phase diagram in Zhang et al. (2011b).

We take several steps to prevent contamination of fluids and microcells. We designed our piping system to be isolated from the ambient environment. By switching three connectors, we can alternate injection and outflow modes of each port without reconnecting tubes. To prevent photodegradation, we wrapped the glass syringes in aluminum foil and covered the entire setup with a black cloth when not taking images. We have set the exposure time as short as possible to protect experimental fluids and fluorescent dye from degradation. We prepared and conducted all stages of the experiments in the same laboratory environment with temperature recorded before and after all the experiments. Despite the "dead volume" of the system being significantly larger than the pore volume, for a single experiment, temperature variation was less than ±0.1°C. For experiments conducted on different days, the temperature variation was ±1°C.

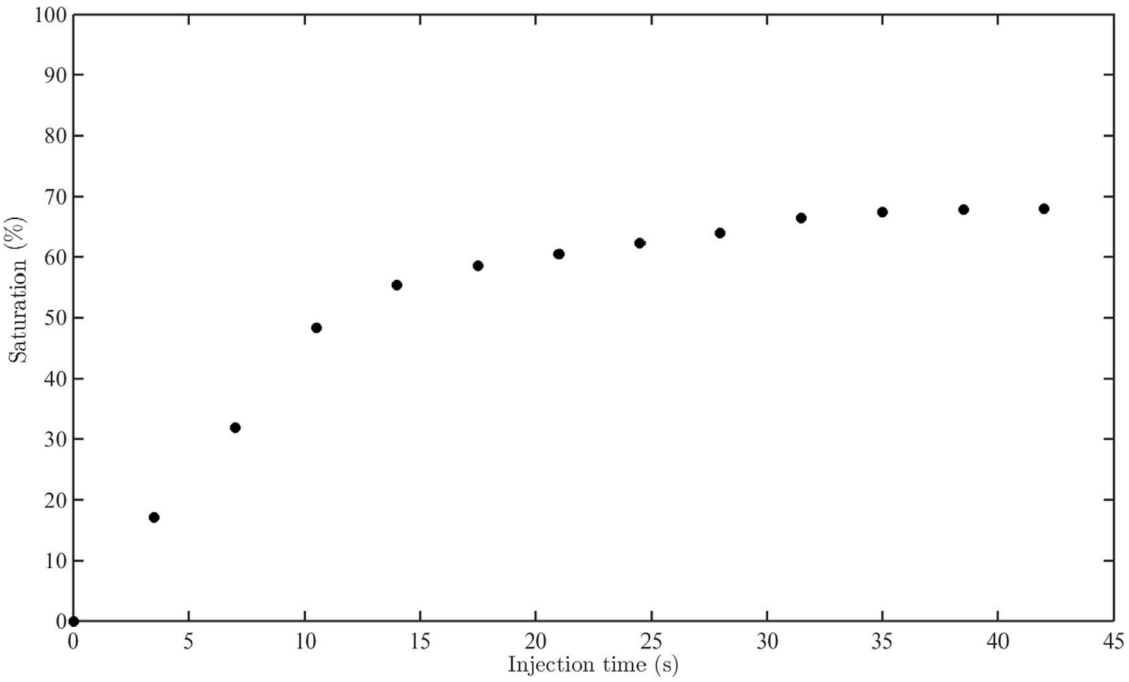

Fig. 4. Saturation vs. time in a test drainage experiment.

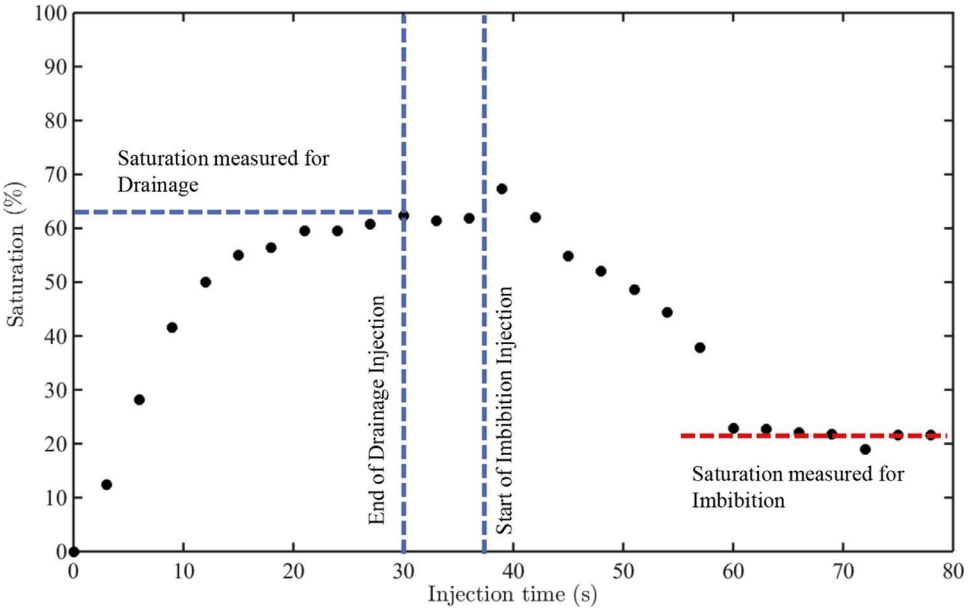

Fig. 5. Saturation vs. injection time in a drainage/imbibition experiment.

3. Experimental results

Fig. 6 shows the results of five experiments in one of the cells (cell D). The first column displays fluids distribution at the drainage cycle end, and the second column displays fluids distribution at the imbibition cycle end. In all experiments at the drainage cycle end, we observe a similar displacement pattern with the injected non-wetting fluid moving through the "preferential flow path" and forming small "side fingers." The main difference between the experiments is the location and size of the side fingers. The displacement patterns at the imbibition cycle end are completely different in these experiments, with different volume of the non-wetting fluid becoming trapped in different locations. Fig. 7 shows the drainage and imbibition patterns observed in five different cells. As in Fig. 6, here the fluid distribution is more repeatable at the drainage cycle end and less repeatable at the imbibition cycle end.

Figs. 8 and 9 show the interface length (in mm) and saturation of the non-wetting fluid at the end of the drainage and imbibition cycles observed in different experiments in all six cells. For this purpose, the system is treated as two-dimensional, i.e., the interface between the two fluids is treated as a curve, and the saturation is defined as the percentage of the pore area occupied by the non-wetting fluid. It is evident that variability in the experiments is higher across different cells than within individual cells, which we attribute to the small deviations in the cells' pore geometry from the design geometry that stems from manufacturing defects.

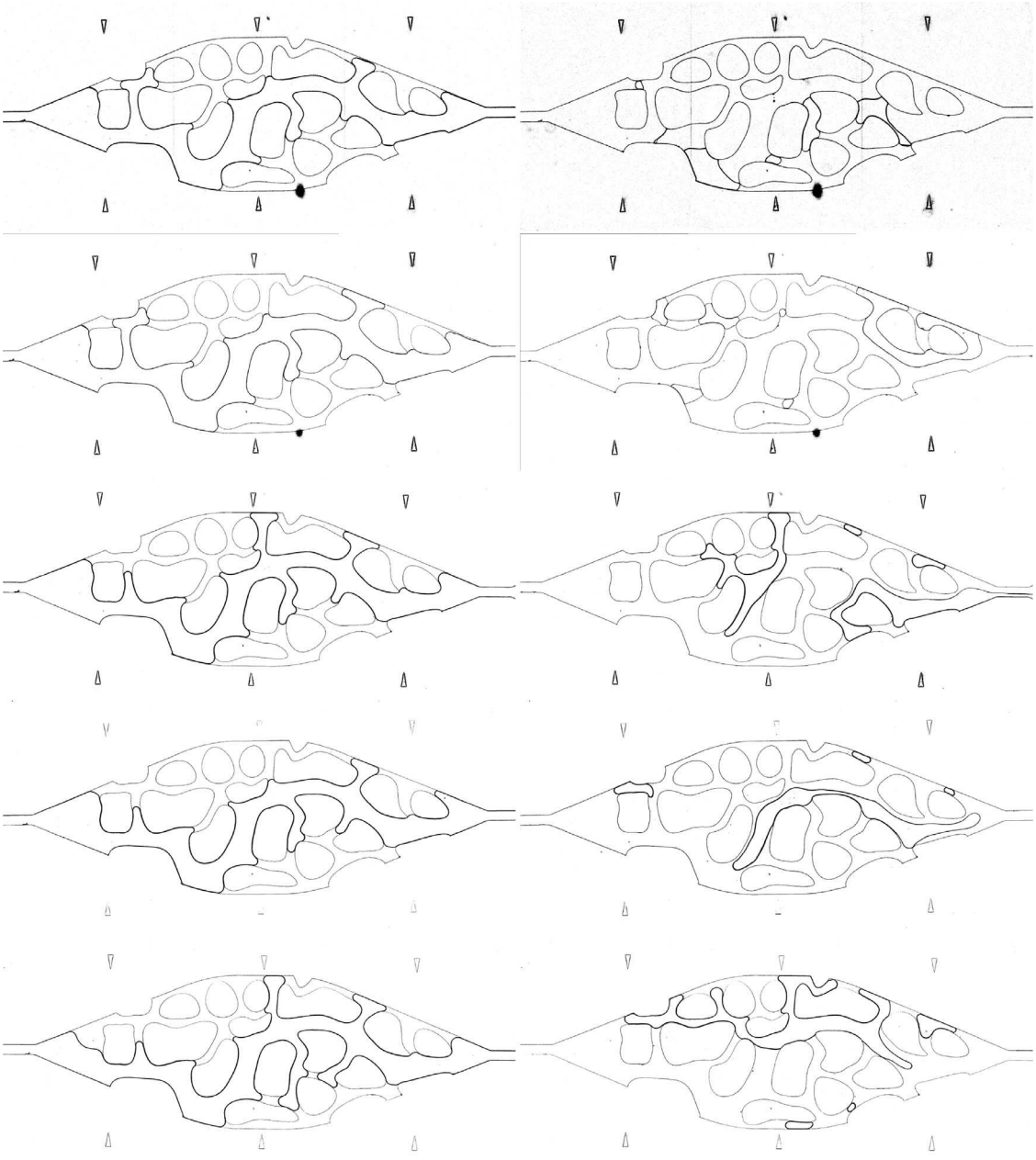

Fig. 6. Five repetitions (first, second, third, fourth, and fifth rows, respectively) of drainage (first column) and imbibition (second column) in the microcell D.

To quantify variability in drainage experiments, we divide the domain in a lattice with indices ξ and η, map the fluid distributions at the end of the drainage cycle, and construct a histogram $p(\xi, \eta)$ of a non-wetting fluid occupying each lattice point (Fig. 10). The histogram shows that the largest variability between the experiments is in the size of the side fingers.

4. Numerical simulations

To understand the source of variability observed in the experiments we model them using the software package STAR-CCM+. We assume that the three-dimensional flow of each fluid phase is governed by a combination of the continuity equation,

$$\nabla \cdot \mathbf{v}_i = 0, \quad i = 1, 2 \tag{1}$$

and the momentum conservation equation,

$$\frac{d\mathbf{v}_i}{dt} = -\frac{1}{\rho_i}\nabla P_i + \frac{\mu_i}{\rho_i}\nabla^2 \mathbf{v}_i, \quad i = 1, 2 \tag{2}$$

subject to the Young–Laplace boundary condition at the fluid-fluid interface:

$$(P_1 - P_2)\mathbf{n} = -(\tau_1 - \tau_2) \cdot \mathbf{n} + \kappa\sigma\mathbf{n} \tag{3}$$

and a no-slip boundary condition at the fluid-solid boundaries. Here, $\tau_i = [\mu_i(\nabla \mathbf{v}_i + \nabla \mathbf{v}_i^{\mathrm{T}})]$ is the viscous stress tensor, $\mathbf{v}_i$ the velocity, P_i is the pressure, and μ_i the viscosity of the ith fluid, κ is the interface curvature, σ is the surface tension, and the normal vector $\mathbf{n}$ points away from the non-wetting phase. In addition, the constant contact angle equal to the static contact angle is prescribed at the fluid-fluid-solid interface. We also consider a two-dimensional approximation of the NS Eqs. (1) and (3):

$$\nabla \cdot \bar{\mathbf{v}}_i = 0, \quad i = 1, 2 \tag{4}$$

and the momentum conservation equation,

$$\frac{d\bar{\mathbf{v}}_i}{dt} = -\frac{1}{\rho_i}\nabla \bar{P}_i + \frac{\mu_i}{\rho_i}\nabla^2 \bar{\mathbf{v}}_i - \frac{12}{h^2}\frac{\bar{\mathbf{v}}_i \mu_i}{\rho_i}, \quad i = 1, 2 \tag{5}$$

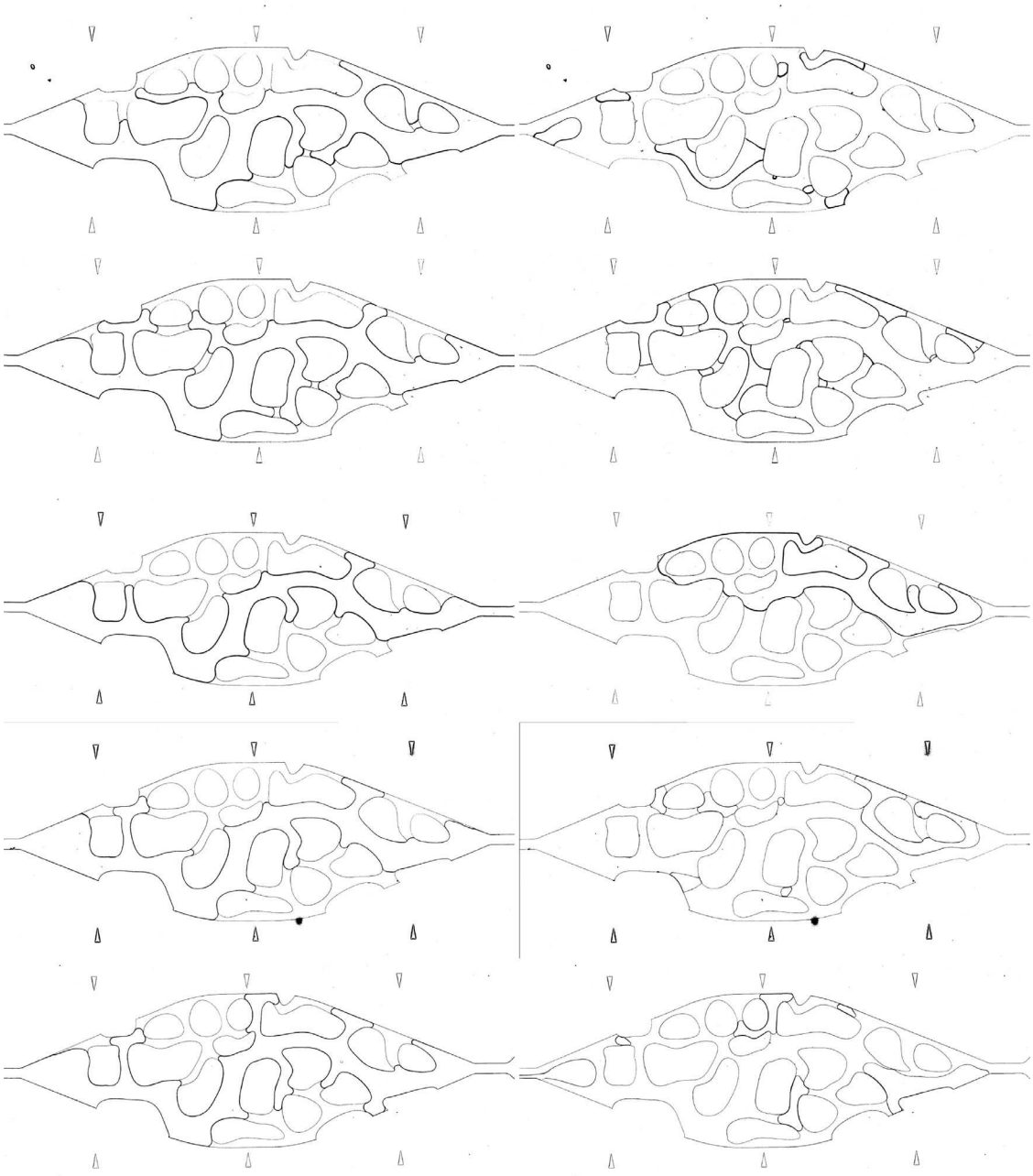

Fig. 7. The second repetition in cell A (first row), cell B (second row), cell C (third row), cell E (forth row), and cell F (fifth row) of drainage (first column) and imbibition (second column).

where over-bar $\bar{*}$ denotes variables averaged over the depth of the microcell. The two- and three-dimensional governing equations are solved with STAR-CCM+, which employs a finite volume discretization on unstructured grids and the volume of fluid method to implicitly track the interface between two fluids. Previous studies (e.g., van Ertbruggen et al., 2008; Yang et al., 2016) have demonstrated the accuracy of STAR-CCM+ for porescale flow modeling.

4.1. Deterministic two- and three-dimensional simulations

It is common to assume that flow in (three-dimensional) microfluidic cells can be accurately described by the two-dimensional NS equations, given that the cell depth is much smaller than the smallest pore throat. To test this assumption for the studied system, we simulate the experiment with a fully resolved three-dimensional model and the corresponding depth-averaged two-dimensional model. The fluids distributions obtained from these simulations are shown in Figs. 11 and 12, respectively.

The two-dimensional simulations have 37,000 elements, and the three-dimensional simulation has 150,000 elements. In both two- and three-dimensional simulations, the time step is 1e−5 s.

We see the same general pattern in the simulations and experiments, i.e., the non-wetting fluid follows the same preferential path as in the experiments. However, we can also see some qualitative differences. In the three-dimensional simulation, the non-wetting fluid completely displaces wetting fluid in the preferential path during the drainage cycle, which is close to what we observe in the experiments. On the other hand, in the two-dimensional simulation, large “lenses” of the wetting fluid are left behind. No such lenses are observed in the experiments. Figs. 8 and 9 show

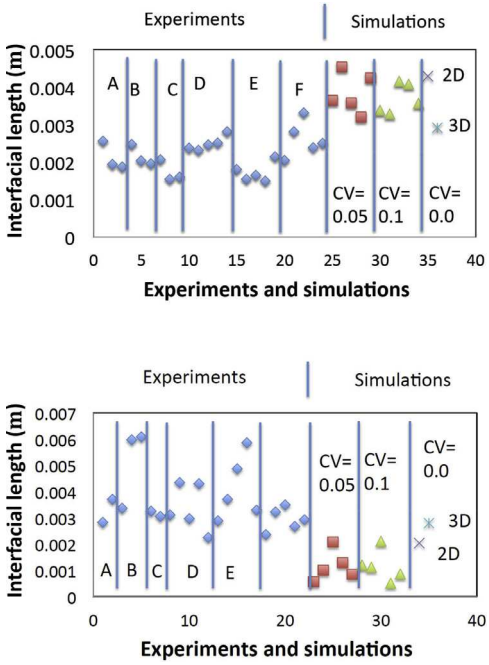

Fig. 8. Interfacial length (m) at the end of the drainage (top) and imbibition (bottom) cycles obtained in the experiments and numerical simulations. Diamond-shaped symbols denote experimental results in A,B,D,E, and F cells; square- and triangle-shaped symbols denote results of the numerical simulations with CV=0.05 and 0.1, respectively; and "×" and "*" denote the deterministic 2D and 3D simulations, correspondingly.

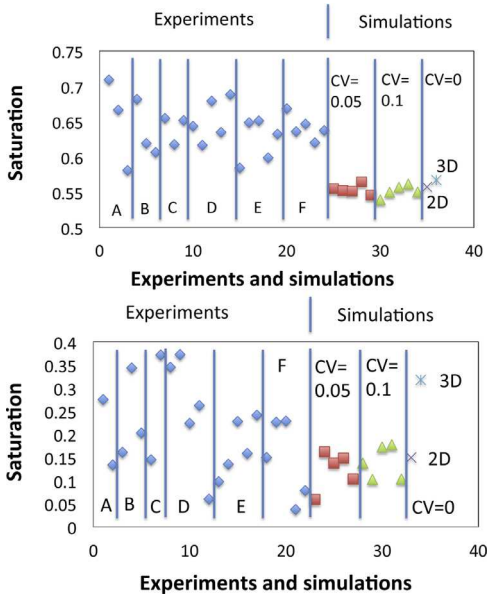

Fig. 9. Saturation of the nonwetting fluid at the end of the drainage (top) and imbibition (bottom) cycles obtained in the experiments and numerical simulations. Diamond-shaped symbols denote experimental results in A,B,D,E, and F cells; square- and triangle-shaped symbols denote results of the numerical simulations with CV=0.05 and 0.1, respectively; and "×" and "*" denote the deterministic 2D and 3D simulations, correspondingly.

the interface length and saturation of the non-wetting fluid at the end of the drainage and imbibition cycles calculated from the two- and three-dimensional simulations. In the three-dimensional simulation, the interface length ($l^d_{3D} = 2.93$ mm) agrees better with the mean interface length in the experiments ($l^d_{exp} = 2.14$ mm) than the interface length in the two-dimensional simulation ($l^d_{2D} =$

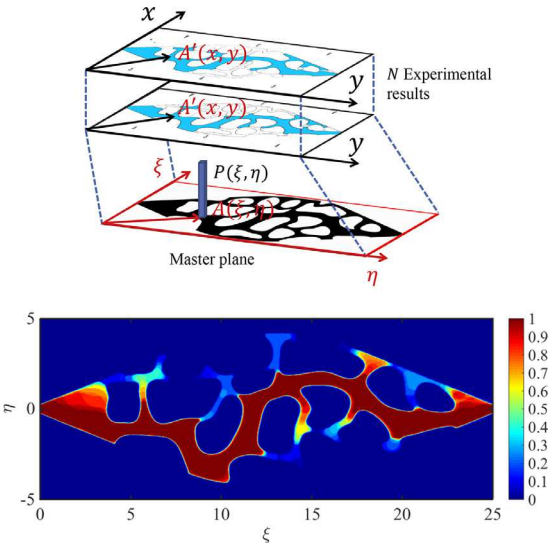

Fig. 10. Top: Definition of the master plane and the mapping process; **Bottom**: $p(\xi, \eta)$ of all the experimental results.

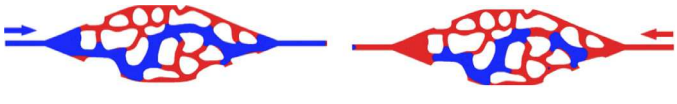

Fig. 11. Three-dimensional simulation of (a) drainage and (b) imbibition with constant injection velocity 9.24×10^{-4} m/s.

Fig. 12. Two-dimensional simulation of (a) drainage and (b) imbibition with constant injection velocity 9.24×10^{-4} m/s.

4.3 mm). The same is true for the saturation results at the drainage cycle end ($S^d_{3D} = 56.75\%$, $S^d_{2D} = 55.78\%$, and $S^d_{exp} = 64.12\%$). Here, mean interface length and mean saturation are defined as the average of interface lengths and saturations over all experiments. For the imbibition cycle, the three-dimensional model is also more accurate in predicting mean interface length ($l^i_{3D} = 2.8$ mm, $l^i_{2D} =$ 2.03 mm, and $l^i_{sim} = 3.6$ mm), but the two-dimensional model is doing a slightly better job for mean saturation ($S^i_{3D} = 31.77\%$, $S^i_{2D} =$ 14.98%, and $S^i_{exp} = 21.13\%$). Given the large variability of the imbibition displacement patterns in the experiments, the latter easily could be a coincidence. Therefore, we conclude that the three-dimensional model describes the experimental results more accurately than the two-dimensional model. We should note that both the two- and three-dimensional models predict significantly larger volumes of the wetting fluid trapped in the "corners" of the preferential path during drainage than observed in the experiments. We attribute this to the fact that because of the manufacturing defects, the corners in the cells are not as sharp as designed (and modeled in the simulations).

4.2. Stochastic two-dimensional simulations

Variability in different experiments in the same cells can be attributed to small variations in the pump injection rate. To

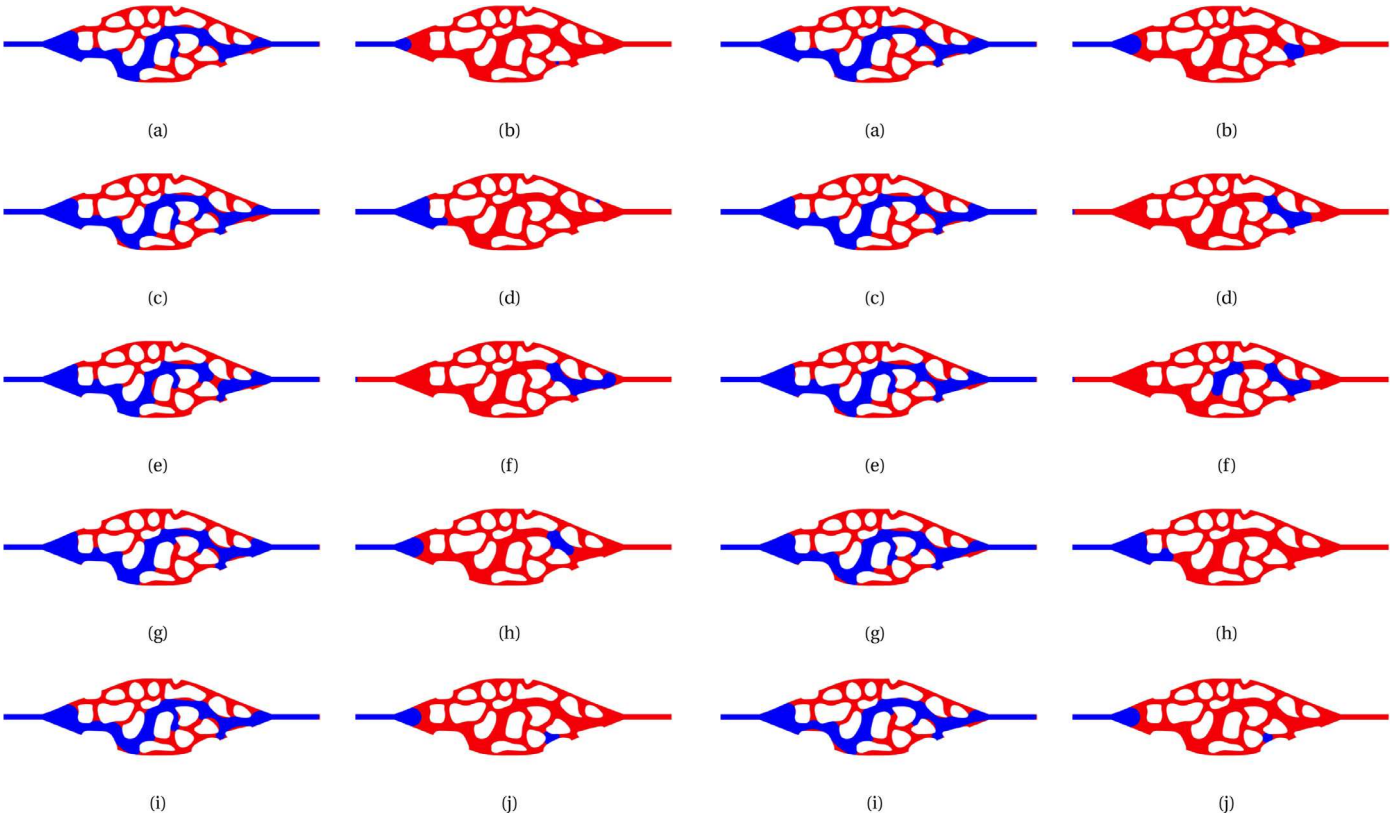

Fig. 13. Two-dimensional simulation of (left column) drainage and (right column) imbibition with random injection velocity with mean 9.24×10^{-4} m/s and CV = 0.05. Different rows are different realizations.

Fig. 14. Two-dimensional simulation of (left column) drainage and (right column) imbibition with random injection velocity with mean 9.24×10^{-4} m/s and CV = 0.1. Different rows are different realizations.

test this hypothesis, we simulate the experiment with a randomly varying injection rate. We conduct two sets of five simulations with the coefficient of variance (CV) of the injection rate ($CV = \sigma_Q/\overline{Q}$, where σ_Q and $\overline{Q}$ are the injection rate standard deviation and mean) set to $CV = 0.05$ (Fig. 13) and 0.1 (Fig. 14).

The coefficient of variance of 0.05 corresponds to the pump accuracy (the syringe pump used in this study has a regular accuracy ±5% based on the flow rate). Because of the high computational cost of the three-dimensional model, we only conduct two-dimensional stochastic simulations. Figs. 13 and 14 show the same pattern as in the experiments. During drainage, the non-wetting fluid saturates the preferential path and forms side fingers, which vary in different (stochastic) simulations. At the imbibition cycle end, there is very high variability in the amount and location of the trapped non-wetting phase. Because imbibition strongly depends on the initial distribution of fluid phases (Herring et al., 2013), it is expected that (small) variations at the end of drainage cycle have led to significant variations in the imbibition pattern. Figs. 8 and 9 show the interface length and saturation of the non-wetting fluid at the end of the drainage and infiltration cycles calculated from the stochastic simulations. Fig. 15 shows the CV of the interface length at the end of the drainage and imbibition cycles obtained in experiments and stochastic simulations. We can see that CV differs for each experimental cell. For the drainage cycle, the CVs obtained from stochastic simulations are within the range of CVs observed in the experiments. For imbibition, the simulations overestimate CV. The simulations with different CVs of the injection rate result in approximately the same CV of the interface length. It is also important to note that the mean interface length and saturation obtained from the stochastic simulations differ from the "mean-field" interface length and

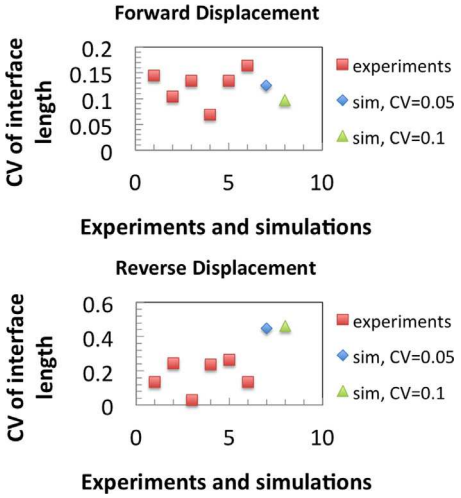

Fig. 15. Coefficient of variance of the interface length at the end of drainage (top) and imbibition (bottom) cycles experimentally observed in six microcells (square symbols) and computed from the stochastic simulations with CV = 0.05 (diamond) and 0.1 (triangle).

saturation obtained from the two-dimensional deterministic simulation. Our results also show that the mean of stochastic simulations agrees better with the average behavior observed in the experiments than the results of the two-dimensional deterministic simulation.

The capillary number in the experiments (and the previously presented simulations) is $Ca = 1.82 \times 10^{-5}$. It is known that instability of immiscible flow increases with the decreasing *Ca*. In Fig. 16, we show the results of five stochastic simulations with

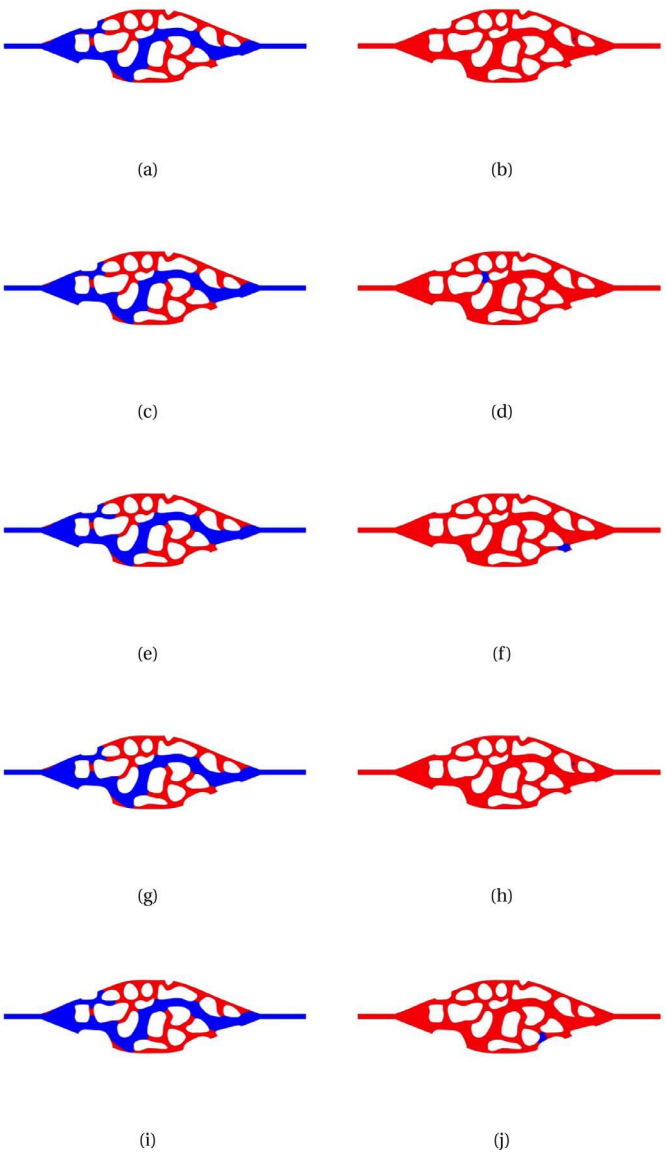

Fig. 16. Two-dimensional simulation of (left column) drainage and (right column) imbibition with random injection velocity with mean 9.24×10^{-1} m/s and CV=0.1. Different rows are different realizations.

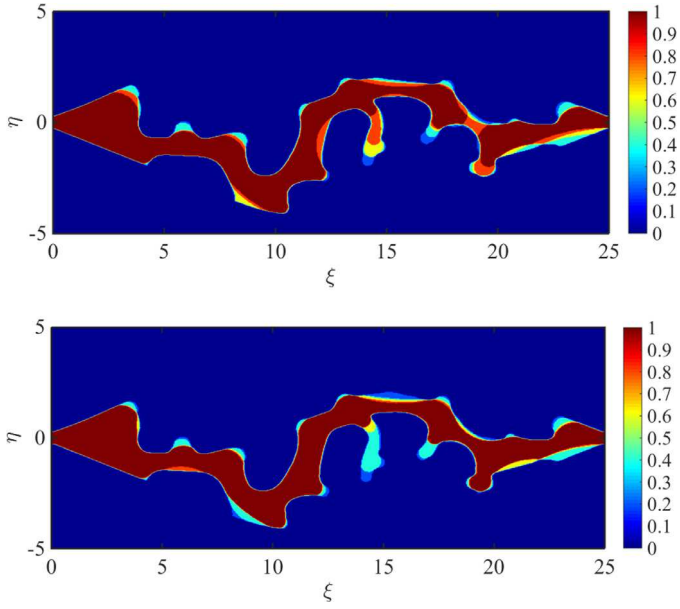

Fig. 17. Top: $p(\xi, \eta)$ of simulation with variance of 0.05; **Bottom**: $p(\xi, \eta)$ of simulation with variance of 0.1.

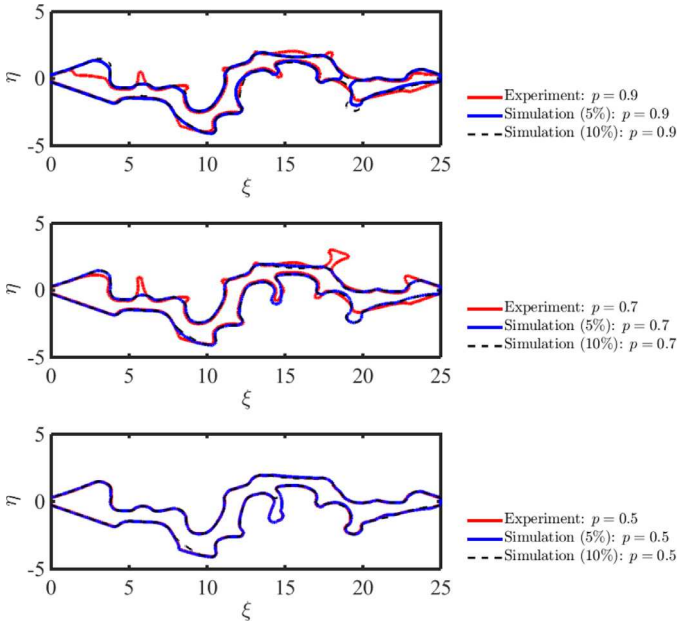

Fig. 18. Contour lines with $p = 0.9$, $p = 0.7$, $p = 0.5$.

$Ca = 1.82 \times 10^{-2}$, which is 100 times larger than in the experiments. The fluid distribution at the displacement cycle end is nearly the same in all simulations. On the other hand, the fluids distribution at the imbibition cycle end significantly varies between simulations, even for this relatively large *Ca*.

The "point-wise" histogram of the non-wetting fluid distribution at the drainage cycle end, obtained from the stochastic simulations, is shown in Fig. 17. As in the experiments, variability in the stochastic simulations is mainly in the side fingers' size. Experiments also exhibit variability in the fluids distribution in the preferential flow path, including breakup and detachment from the solid grains of the non-wetting fluid in some simulations. Unexpectedly, the variability is more pronounced in the simulations with the smaller variance of the injection rate.

In Fig. 18, we compare the contour lines of simulation and experimental histograms for several p values. There is a significant difference between the simulation and experimental $p = 0.9$ contour lines. Specifically, the numerical model underestimates the size of side fingers and over-predicts thickness of the "residual" wetting fluid film left on the obstacles forming the preferential flow path. Contour lines corresponding to $p = 0.5$ and 0.7 agree within 5% for the side fingers at the lower part of the domain, but they disagree for the upper side fingers. A similar comparison (Fig. 19) between the deterministic simulations and experimental results shows that the three-dimensional simulation predicts the experimental results more accurately than the two-dimensional simulation. For example, the three-dimensional simulation accurately predicts that there is virtually no wetting fluid film left on the obstacles forming the preferential flow path.

5. Conclusions

The reproducibility of porescale multiphase flow experiments with small capillary number ($Ca = 1.82 \times 10^{-5}$) was investigated in a microfluidic device. Six replicas of the devise were manufactured

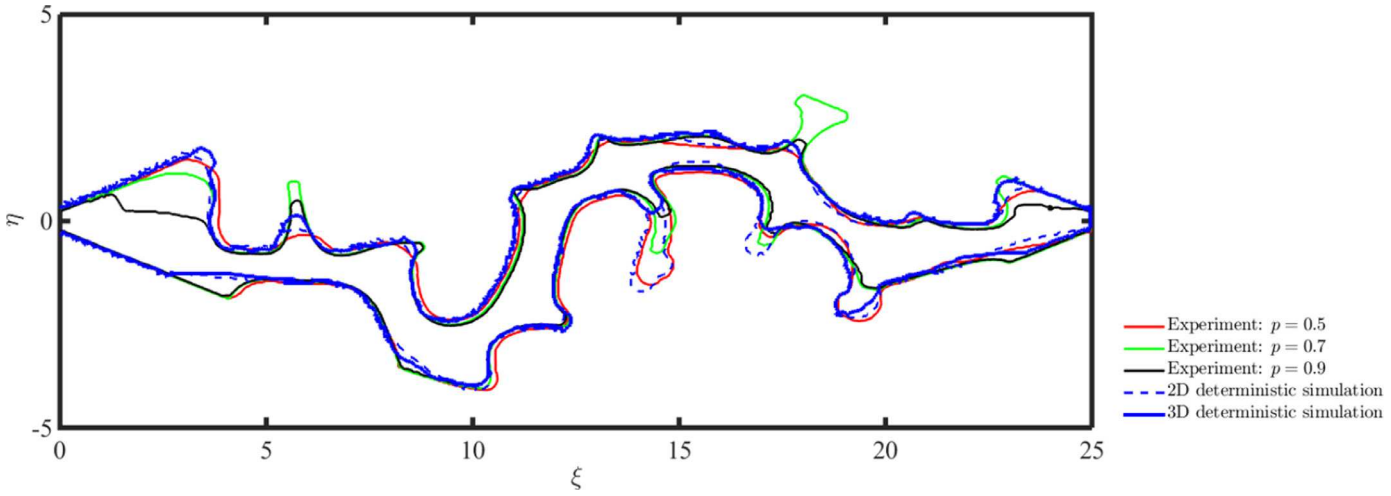

Fig. 19. Contour lines comparison between the deterministic simulations and the experimental results with different p values.

and up to five experiments were conducted in each replica. During drainage stage, we observed smaller variability in experiments performed in the same cell than in experiments conducted in different cells. Even greater variation in the experimental results were noted at the imbibition cycle end.

Numerical simulations using the same parameters as the experiments were performed in the exact same geometry both in two and three dimensions. To reveal the impact of fluctuations in the pumping flow rate, we simulated the flow both deterministically and statistically. We found that the deterministic three-dimensional model is more accurate than the two-dimensional model.

Randomly varying (in time) the injection rate quantitatively captured the variability observed in the experiments. The average behavior of stochastic simulations was in better agreement from the corresponding deterministic simulation and better agrees with the average behavior observed in the experiments.

For the larger capillary number ($Ca = 1.82 \times 10^{-2}$), we observed nearly zero variability in the results of stochastic numerical simulations of the drainage cycle, suggesting that the drainage experiments could be "reproducible" for higher *Ca*. Variability in the imbibition results remained high, even for this relatively large *Ca*. To confirm our conclusion that higher *Ca* is needed to obtain reproducible experimental results, additional experimental studies are needed.

Acknowledgments

I. Battiato gratefully acknowledges partial support by the U.S. Department of Energy (DOE), Office of Biological and Environmental Research, Subsurface Biogeochemical Research (SBR) Program through the SBR Scientific Focus Area at Pacific Northwest National Laboratory (PNNL), and the National Science Foundation (NSF). A. Tartakovsky was partially supported by the U.S. Department of Energy (DOE) Office of Advanced Scientific Computing (ASCR) as part of the Early Career Award "New Dimension Reduction Methods and Scalable Algorithms for Multiscale Nonlinear Phenomena." PNNL is operated by Battelle for the DOE under Contract DE-AC05-76RL01830.

References

Bandara, U., Tartakovsky, A., Oostrom, M., Palmer, B., Grate, J., Zhang, C., 2013. Smoothed particle hydrodynamics pore-scale simulations of unstable immiscible flow in porous media. Adv Water Resour 62 (Part C (0)), 356–369.
Blunt, M.J., 2001. Flow in porous media – pore-network models and multiphase flow. Curr. Opin. Colloid Interface Sci. 6 (3), 197–207.
Cottin, C., Bodiguel, H., Colin, A., 2010. Drainage in two-dimensional porous media: from capillary fingering to viscous flow. Phys. Rev. E 82 (4), 046315.
Ferrari, A., Jimenez-Martinez, J., Borgne, T.L., Méheust, Y., Lunati, I., 2015. Challenges in modeling unstable two-phase flow experiments in porous micromodels. Water Resour. Res. 51 (3), 1381–1400.
Hassanizadeh, S.M., Gray, W.G., 1990. Mechanics and thermodynamics of multiphase flow in porous media including interphase boundaries. Adv. Water Resour. 13 (4), 169–186.
Herring, A.L., Harper, E.J., Andersson, L., Sheppard, A., Bay, B.K., Wildenschild, D., 2013. Effect of fluid topology on residual nonwetting phase trapping: implications for geologic co 2 sequestration. Adv. Water Resour. 62, 47–58.
Hirt, C.W., Nichols, B.D., 1981. Volume of fluid (vof) method for the dynamics of free boundaries. J. Comput. Phys. 39 (1), 201–225.
Lenormand, R., Touboul, E., Zarcone, C., 1988. Numerical models and experiments on immiscible displacements in porous media. J. Fluid Mech. 189, 165–187.
Lenormand, R., Zarcone, C., Sarr, A., 1983. Mechanisms of the displacement of one fluid by another in a network of capillary ducts. J Fluid Mech 135, 337–353.
Liu, H., Valocchi, A.J., Werth, C., Kang, Q., Oostrom, M., 2014. Pore-scale simulation of liquid co 2 displacement of water using a two-phase lattice boltzmann model. Adv. Water Resour. 73, 144–158.
Meakin, P., Tartakovsky, A.M., 2009. Modeling and simulation of pore-scale multiphase fluid flow and reactive transport in fractured and porous media. Rev. Geophys. 47 (3). RG3002.
Miller, C.T., Christakos, G., Imhoff, P.T., McBride, J.F., Pedit, J.A., Trangenstein, J.A., 1998. Multiphase flow and transport modeling in heterogeneous porous media: challenges and approaches. Adv. Water Resour. 21 (2), 77–120.
Pan, C., Hilpert, M., Miller, C.T., 2004. Lattice-boltzmann simulation of two-phase flow in porous media. Water Resour. Res. 40 (1), W01501.
Sahimi, M., 2011. Flow and Transport in Porous Media and Fractured Rock: From Classical Methods to Modern Approaches. John Wiley & Sons.
Steinbach, I., Pezzolla, F., Nestler, B., Seeßelberg, M., Prieler, R., Schmitz, G.J., Rezende, J.L.L., 1996. A phase field concept for multiphase systems. Physica D 94 (3), 135–147.
Tartakovsky, A.M., Panchenko, A., 2016. Pairwise force smoothed particle hydrodynamics model for multiphase flow: surface tension and contact line dynamics. J. Comput. Phys. 305, 1119–1146.
van Ertbruggen, C., Corieri, P., Theunissen, R., Riethmuller, M.L., Darquenne, C., 2008. Validation of CFD predictions of flow in a 3D alveolated bend with experimental data. J. Biomech. 41 (2), 399–405.
Wachem, B.V., Almstedt, A.-E., 2003. Methods for multiphase computational fluid dynamics. Chem. Eng. J. 96 (1), 81–98.
Yang, X., Mehmani, Y., Perkins, W.A., Pasquali, A., Schünherr, M., Kim, K., Perego, M., Parks, M.L., Trask, N., Balhoff, M.T., Richmond, M.C., Geier, M., Krafczyk, M., Luo, L.-S., Tartakovsky, A.M., Scheibe, T.D., 2016. Intercomparison of 3D pore-scale flow and solute transport simulation methods. Adv. Water Resour. 95, 176–189.
Young, T., 1805. An essay on the cohesion of fluids. Philos. Trans. R. Soc. London 95, 65–87.
Zhang, C., Oostrom, M., Grate, J.W., Wietsma, T.W., Warner, M.G., 2011a. Liquid co2 displacement of water in a dual-permeability pore network micromodel. Environ. Sci. Technol. 45 (17), 7581–7588.
Zhang, C., Oostrom, M., Wietsma, T.W., Grate, J.W., Warner, M.G., 2011b. Influence of viscous and capillary forces on immiscible fluid displacement: pore-scale experimental study in a water-wet micromodel demonstrating viscous and capillary fingering. Energy Fuels 25 (8), 3493–3505.